Cross-Linking PEG Microgels with Mesoporous Organosilica Nanoparticles to Engineer Microporous Annealed Particle Scaffold Properties

ACS OMEGA

Open Access

http://pubs.acs.org/journal/acsodf

Article

Cross-Linking PEG Microgels with Mesoporous Organosilica Nanoparticles to Engineer Microporous Annealed Particle Scaffold Properties

Jonathan M. Zuidema,* Alessandro Ajò, Marco Carofiglio, and Luisa De Cola*

Cite This: *ACS Omega* 2026, 11, 746−756

Read Online

ACCESS | Metrics & More | Article Recommendations | Supporting Information

ABSTRACT: Microporous annealed particle (MAP) scaffolds composed of cross-linked microgels are emerging as important biomaterials due to their modular design, high porosity, and large surface area, which allow for highly tailored properties, cellular infiltration, nutrient and waste exchange, and improved drug release characteristics. To further expand on these technologies and enhance their modular design, thiolated mesoporous organosilica nanoparticles (ssMSN-SH), which degrade in response to glutathione, were first cross-linked inside of 4-arm poly(ethylene glycol) maleimide microgels. The microgel size, rheological properties, and payload release characteristics were determined. Hierarchical MAP scaffolds were then created by cross-linking 4-arm poly(ethylene glycol) maleimide microgels with ssMSN-SH. Surface attachment and cross-linking of microgels using ssMSN-SH were confirmed with scanning electron microscopy and confocal imaging; rheological properties were characterized; porosity was analyzed; glutathione-induced degradation of MAP scaffolds was determined; and the depth of viable NIH/3T3 fibroblasts into MAP scaffolds was visualized using confocal microscopy. ssMSN-SH cross-linked microgels form MAP scaffolds with an increase in the storage modulus, maintain their porosity while decreasing the interparticle distance, degrade in response to glutathione, and increase the depth of viable NIH/3T3 fibroblasts into scaffolds when compared with bulk PEG hydrogels.

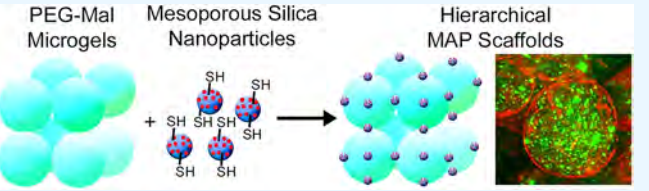

INTRODUCTION

Microgels, hydrogel microparticles ranging in size roughly between ∼1 and 100 μm, possess several advantageous characteristics for biomedical applications when compared to bulk hydrogels. These include shear-thinning-enabled injectability, microporosity between particles allowing for cellular infiltration, and large surface areas for cell attachment and increased permeation of released therapeutics through injection sites.[1] They are highly tunable; their mesh size, particle size, packing density, and porosity can be tailored; and their mechanical properties can be adjusted based on polymer concentrations and selection.[2,3] Importantly, by jamming microgels to make them densely packed, they can be formed into macroscopic granular hydrogels.[4−6] The properties of granular hydrogels depend on the microgel composition and interparticle interactions, and densely packed microgels can be cross-linked together to form microporous annealed particle (MAP) scaffolds.[7−10] MAP scaffolds are especially attractive for tissue engineering because they can achieve macroscopic architectures while maintaining microscale porosity for cellular integration, waste exchange, and therapeutic delivery throughout the scaffold.[11] While microgels, granular hydrogels, and MAP scaffolds have great potential in tissue engineering due to their modular nature, nanoparticles have been added into their designs to further increase functionalities and precisely tune the properties of microgels.[12−14] Specifically, silica-based nanoparticles are useful for incorporation into microgels as they can be fabricated with pores for drug loading, their surfaces are readily functionalized, and their size and morphology can be tailored on demand.[15]

Mesoporous silica nanoparticles (MSNs) are widely produced via the surfactant-templating approach, which allows for controlled formation of mesostructures, morphologies, and dimensions.[16] MSN biocompatibility, high specific surface areas, tunable pore sizes, and stable porous structures have driven their use in drug delivery applications.[17] Recent advancements have created breakable MSNs through the incorporation of various moieties into the silica network. These include bispropyldisulfide as a redox-sensitive group,[18,19] bis-alkoxysilanes for breakability with UV,[20] nucleic acids for enzymatic degradation,[21] and pH-responsive iron-doped MSNs.[22] The ease of surface modifications using silane chemistries can produce MSNs coated with thiols, amino groups, polyethylene glycols (PEG), aptamers, antibodies, and targeting peptides.[23−25] These valuable properties, as well as

Received: July 17, 2025
Revised: December 5, 2025
Accepted: December 15, 2025
Published: December 19, 2025

the stability of MSNs, have led to their incorporation into hydrogels in order to wield more control over hydrogel properties.[26,27] MSNs have been incorporated into many different hydrogel types for biomedical applications, including injectable polyamidoamine, PEG, alginate, chitosan, and hyaluronic acid-based hydrogels.[28−33] This has allowed for precision drug release, self-healing, specialized cross-linking, and cell-responsive degradation. Because of the versatility and increased functionality provided by MSNs, this study employs MSNs, specifically thiolated mesoporous organosilica nanoparticles (ssMSN-SH), as cross-linkers and modifiers of microgels and MAP scaffolds.

With the continued rise in the use of granular hydrogels and MAP scaffolds in therapeutic delivery, tissue engineering, and regenerative medicine, there is promise in incorporating nanoparticles with these biomaterials to tailor the granular hydrogel and MAP scaffold properties. PEG is one of the most common synthetic, biocompatible polymers in tissue engineering, and it was chosen here due to the highly tailorable reactive groups that can cap the ends of PEG chains for cross-linking reactions.[34,35] We specifically chose PEG-maleimide (PEG-Mal) microgels as they have previously been shown to form microgels that support cellular infiltration, have tailorable mechanical properties, and can readily undergo maleimide−thiol chemistry for attachment of other molecules.[36−38] Here, we report the inclusion of ssMSN-SH with PEG-Mal cross-linked microgels in two different formats: (1) incorporation of ssMSN-SH inside of microgels during fabrication and (2) ssMSN-SH as PEG-Mal microgel interparticle cross-linkers to form MAP scaffolds. Importantly, using maleimide−thiol cross-linking, we were able to create and characterize hierarchical MAP scaffolds that have an increased storage modulus, glutathione-induced degradation, and a decreased interparticle distance and that increase the depth of viable NIH/3T3 fibroblasts into scaffolds.

MATERIALS AND METHODS

Synthesis of Mesoporous Organosilica Nanoparticles (ssMSNs). Nanoparticles were fabricated in a manner similar to previous reports, and 20 mL of DIH_2O was added to a 50 mL round-bottom flask and heated to 90 °C.[18,32] 600 mg (1.65 mM) of hexdecyltrimethylammonium bromide (CTAB, 98%, Sigma-Aldrich, H5882) and 60 mg (0.4 mM) of triethanolamine (TEA, 99%, Sigma-Aldrich, 90279) were then added, and the solution was stirred at 200 rpm for 20 min under reflux. 1.276 g (2.69 mM) of Bis(triethoxysilyl propyl)disulfide (BTDS, 95%, Fluorochem, S02135) and 0.8397 g (4.03 mM) of tetraethyl orthosilicate (TEOS, 99%, Sigma-Aldrich, 86578) were then added dropwise and stirred at 200 rpm for an additional hour at 90 °C under reflux to form nanoparticles. The solution was then removed from heat, pelleted via centrifugation (35,000 RCF, 20 min, 20 °C), and washed three times in EtOH. The CTAB template was removed via reflux overnight in a solution of EtOH (12 mL) and HCl (1.6 mL, 38% HCl). Particles were then collected via centrifugation (35,000 RCF, 30 min, 20 °C) and washed 1× in ethanol, 1× in 50:50 DIH_2O/EtOH, and 1× in DIH_2O.

Synthesis of Mesoporous Organosilica Nanoparticles with Thiol Functionalization (ssMSN-SH). 10 mg of lyophilized mesoporous organosilica nanoparticles (ssMSNs) were resuspended in 1 mL of toluene. 12 μL (64.6 μM) of (3-mercaptopropyl) trimethoxysilane (95%, Sigma-Aldrich, 175617) and 1 μL (1.124 mM) of TEA were added, and the solution was mixed overnight at RT (25 °C). ssMSN-SH were then washed 1× in toluene, 1× in 50:50 EtOH:toluene, 1× in EtOH, 1× in 50:50 EtOH:DIH_2O, and 1× in DIH_2O.

Rhodamine B Isothiocyanate Loading of Organosilica Nanoparticles. To load ssMSNs with rhodamine B isothiocyanate (Sigma-Aldrich, 283924), a previous protocol was adapted.[12] 5 mg of ssMSNs were suspended in a solution of 5 mg (9.32 μM) of rhodamine B isothiocyanate in 1 mL of DIH_2O. The suspension was vigorously stirred for 4 h in the dark. Subsequently, the solvent was evaporated, and the particles were washed 1× in H_2O, 1× in H_2O:EtOH, 1× in EtOH, 1× in 50:50 EtOH:toluene, and 1× in toluene. Rhodamine B isothiocyanate-loaded ssMSNs were then functionalized with thiols as described above. The loading of rhodamine B isothiocyanate was determined using a Tecan Infinite M200 plate reader (λ_{ex}: 570 nm, λ_{em}: 595 nm) following particle breaking via incubation at 37 °C in PBS at pH 7 containing 100 mM L-glutathione reduced (GSH) (Sigma-Aldrich, G4251), and it was found to be 4.2 ± 0.6% by mass of ssMSN.

Characterization of ssMSNs. The hydrodynamic particle size (dynamic light scattering, DLS) and ζ-potential were measured with a Malvern Zetasizer Ultra instrument equipped with a HeNe laser (633 nm) and a Peltier thermostatic system in water at 25 °C. Thermogravimetric analysis (TGA) was conducted on pristine ssMSNs and ssMSN-SH using a Netzsch model STA 449 fi Jupiter instrument. The samples were kept at 100 °C for 30 min for stabilization and then heated from 130 to 800 °C at a speed of 10 °C min^{-1}. The analysis was carried out under a 20 mL min^{-1} airflow. The N_2 adsorption/desorption profile was determined by using a Micromeritics ASAP 2020 surface area and porosity analyzer. Small-angle X-ray scattering was conducted with the SAXSess mc2 instrument (Anton Paar GmbH) containing a slit collimator system and the PW3830 laboratory X-ray generator (40 kV, 50 mA) with a long-fine focus sealed X-ray tube (Cu Kα λ = 0.1542 nm) from PAN Analytical. Detection was performed with the 2D imaging plate reader Cyclon by PerkinElmer. Measurements were performed on lyophilized samples for 10 min. The 2D data were converted to 1D data and the background was corrected by using SAXSQuant software (Anton Paar GmbH). Transmission electron microscopy was conducted using a Talos L10C (FEI) electron microscope.

Poly(ethylene glycol) Microgel Synthesis. Microgel fabrication was adapted from previous reports,[8,10] where a solution of mineral oil (Sigma-Aldrich, 330779) and 2% Span 80 (Sigma-Aldrich, S6760) was added to a 50 mL conical tube. 20% by mass (0.5 μM) of 4-arm polyethylene glycol (PEG) maleimide (MW 40000 Da, JenKem, JKA7067) was dissolved in pH 5.0 MES buffer (Thermo Scientific, J61960.AP). In another tube, HS-PEG-SH (MW 1500 Da, JenKem, JKA4105) was dissolved in pH 5.0 MES buffer at different molar ratios that were calculated to allow for either 2-arm, 3-arm, or 4-arm PEG-maleimide to be cross-linked. 100 μL of 20% (m/m) (0.5 μM) 4-arm PEG-maleimide was then combined with 100 μL of 0.5 μM (2-arm), 0.75 μM (3-arm), or 1.0 μM (4-arm) HS-PEG-SH for a final concentration of 10% (m/m) 4-arm PEG-maleimide. This 200 μL of the combined PEG solution was then added to a 30× volume mineral oil/2% Span 80 solution and vortexed for 20 s to create the emulsion. The microgels were then placed on a shaker and allowed to cross-link over 30 min. Cross-linked microgels were collected via centrifugation at 4000 RCF for 5 min and washed 1× with 0.3% Triton-X 100

https://doi.org/10.1021/acsomega.5c07004
ACS Omega 2026, 11, 746−756

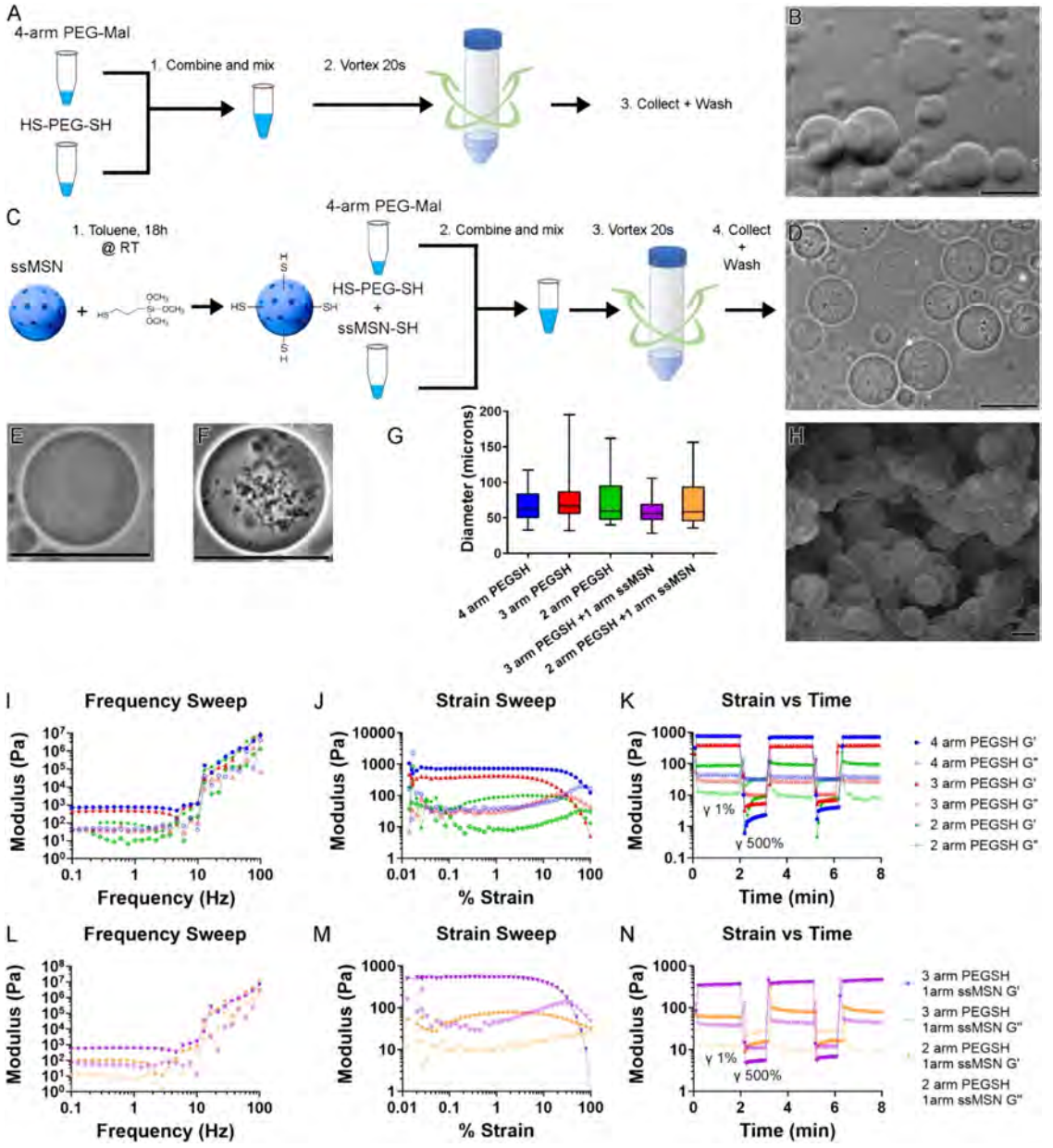

Figure 1. Microgel fabrication and mechanical properties. (A) 4-arm PEG-Mal was combined with SH-PEG-SH in a batch emulsion to create (B) control microgels (scale = 100 μm). (C) Thiolated ssMSNs were incorporated into the SH-PEG-SH solution and then (D) made via a batch emulsion (scale = 100 μm). Higher-magnification images of the (E) control (scale = 100 μm) and (F) ssMSN-SH-incorporated (scale = 100 μm) microgels. (G) Microgel size analysis. Data are displayed as a box and whisker plot with the Min and Max, upper quartile, median, and lower quartile. (H) SEM micrograph of lyophilized microparticles (scale = 10 μm). (I) Frequency and (J) strain sweeps were performed on microgels that had 4-arm, 3-arm, and 2-arm molecular equivalents of Mal groups cross-linked, and decreasing the amount of PEG-Mal arms cross-linked reduced the storage modulus (G') of the microgels. (K) Cyclic strain (1% strain at low-strain regions and 500% strain for high-strain regions) demonstrate the thixotropic properties of the microgels, as they return to their initial storage modulus following increased strain. (L) Frequency and (M) strain sweeps were performed on microgels that had 1-arm cross-linked with ssMSN-SH and either 3-arm or 2-arm molecular equivalent of Mal groups cross-linked. Decreasing the amount of PEG-Mal arms cross-linked reduced the storage modulus (G') of the microgels. (N) Cyclic strain (1% strain at low-strain regions and 500% strain for high-strain regions) demonstrate the thixotropic properties of the ssMSN-SH microgels, as they return to their initial storage modulus following increased strain.

(Sigma-Aldrich, ×100) in H_2O, 1× in 50:50 acetone:H_2O, 1× in H_2O, and 1× in PBS.

PEG ssMSN-SH Microgel Synthesis. PEG + ssMSN-SH microgels were fabricated in a manner similar to that described above, with small alterations to add ssMSN-SH or rhodamine-loaded ssMSN-SH. TGA was used to quantify the moles of SH on the surface of the ssMSNs, and the quantity of particles that contain 0.5 μM of (3-mercaptopropyl) trimethoxysilane (amount to couple to 1-arm of the maleimide 4-arm PEG) were suspended in the 100 μL of HS-PEG-SH solution. This was then mixed with 100 μL of 20% 4-arm PEG-maleimide, and cross-linking and washing steps were conducted as described above.

Fabrication of MAP Scaffolds of PEG Microgels Cross-Linked with ssMSN-SH. PEG microgels were fabricated with 75% (3 of the 4) maleimide arms cross-linked with HS-PEG-

https://doi.org/10.1021/acsomega.5c07004
ACS Omega 2026, 11, 746−756

SH. This leaves 1-arm of maleimide free to undergo further cross-linking. These gels were then centrifuged for 5 min at 4000 RCF, and the supernatant was removed. ssMSN-SH suspended in PBS at 2 mg mL^{-1} were added to centrifuged microgels to cross-link into MAP scaffolds for 15 min at RT. The MAP scaffolds were then washed 3× with PBS to remove any remaining ssMSN-SH that were not cross-linked.

Characterization of Microgels and Multiscale MAP Scaffolds. Rheological measurements were conducted by using a Thermo Scientific HAAKE modular advanced rheometer system (MARS). Microgels were centrifuged for 5 min at 4000 RCF, the supernatant was removed, and the microgels were then transferred to the rheometer plate. All measurements were conducted at 37 °C, using an 8 mm geometry and a 0.5 mm gap size (n = 3). Frequency sweeps were conducted from 0.1 to 100 Hz at a constant 1% strain, while strain sweeps were conducted from 0.1 to 100% strain and at a constant frequency of 1 Hz. Cyclic strain measurements were then conducted between low (1%) and high (500%) strains over 120 and 60 s, respectively, and repeated 3 times at a constant frequency of 1 Hz similar to established protocols.[10] Rhodamine B isothiocyanate release was determined using a Tecan Infinite M200 plate reader (λ_{ex}: 570 nm, λ_{em}: 595 nm) following particle breaking via incubation at 37 °C in PBS at pH 7 containing 100 mM GSH. The supernatant was collected on indicated time points and replaced at each time point. Degradation products of ssMSN-cross-linked MAP scaffolds were imaged with bright-field microscopy using an Olympus IX 71 microscope. Fluorescence images were acquired with an Olympus IX 71 microscope. In order to determine the MAP scaffold porosity, microgels were centrifuged for 5 min at 4000 RCF. Microgels were then transferred to a 96-well plate and again centrifuged at 1000 RCF for 5 min to evenly distribute themselves. ssMSN-SH were then added in PBS at a concentration of 2 mg mL^{-1} for the cross-linked MAP scaffolds. Then, a high-molecular-weight solution of fluorescein isothiocyanate-dextran (0.1 mg mL^{-1} in PBS) (2000 kDa, Sigma-Aldrich, FD2000S) was incubated in the microgel scaffolds for 1 h. Confocal images were then acquired by using a Nikon Ti2 Eclipse A1 laser confocal microscope. The images were binarized and watershed and particles were analyzed using the FIJI distribution of ImageJ according to published protocols.[10] The area and major axis lengths for each pore were then averaged across both microgel and ssMSN-cross-linked microgel granular hydrogels (n = 3). Scanning electron microscopy was conducted using a FE-SEM Sigma (Zeiss) instrument with an in-lens detector (2 kV and 3.5 WD).

Culture of NIH/3T3 Murine Fibroblasts. For cell culture experiments, microgels were centrifuged for 5 min at 4000 RCF. Microgels were then transferred to a 96-well plate and again centrifuged at 1000 RCF for 5 min to evenly distribute themselves. For ssMSN-SH-cross-linked scaffolds, ssMSN-SH were then added in PBS at a concentration of 2 mg mL^{-1} for the cross-linked MAP scaffolds. These were gently washed three times in DMEM (GIBCO) and soaked in DMEM containing 10% fetal bovine serum (FBS, Gibco), 1% L-glutamine (Euroclone), and 1% penicillin−streptomycin (Euroclone, 100 μg mL^{-1} streptomycin and 100 units/mL penicillin) for 1 h prior to cell seeding. Bulk hydrogels were cross-linked from the solution prior to seeding and soaked in DMEM containing 10% FBS, 1% L-glutamine, and 1% penicillin−streptomycin for 1 h prior to seeding. NIH/3T3 murine fibroblasts (ATCC) were seeded at a density of 20k cells per well in the 96-well plates in DMEM (Gibco) containing 10% FBS, 1% L-glutamine, and 1% penicillin−streptomycin. After 24 h in culture (37 °C, 5% CO_2 atmosphere), live cells were stained with calcein AM (Invitrogen, C1430), and dead cells were stained with propidium iodide (ThermoFisher, P3566) and washed 1× in PBS. Cells were imaged using a Nikon Ti2 Eclipse A1 laser confocal microscope. The cellular depth into granular hydrogels (n = 5) was determined using ImageJ. The maximum distance of viable NIH/3T3 fibroblasts was determined in 5 slices per scaffold, and this was also compared to the bulk hydrogel depth (10% w/w 4-arm PEG-maleimide cross-linked with HS-PEG-SH).

Statistical Analysis. Statistical analysis was performed using GraphPad Prism (10.2.3). Multiple groups were analyzed using one-way ANOVA and Tukey's posthoc test conducted with $p < 0.05$. As shown in Figure 4, Student's t test was used to determine the differences between the two groups.

RESULTS AND DISCUSSION

ssMSN-SH-Containing Microgels. ssMSNs were synthesized using the sol−gel method as previously described and detailed in the methods.[39] This process created spherical ssMSNs with an average diameter of ∼90 nm, a ζ-potential of −38 ± 1.2 mV, and a peak pore diameter of 3 nm (Figures S1 and S2). Thiol groups were incorporated onto the surface of the ssMSNs via reaction of ssMSNs with (3-mercaptopropyl) trimethoxysilane in a solution of toluene and triethanolamine overnight, creating spherical ssMSN-SH of diameters ∼90 nm and a ζ-potential of −38.2 ± 0.87 mV (Figure S1). Thermogravimetric analysis showed conjugation with (3-mercaptopropyl) trimethoxysilane totaling 10% by mass with this process (Figure S3). Once synthesized, ssMSN-SH were incorporated into microgels during fabrication. Control microgels were created using the oil:water emulsion technique as described in the Supplementary Methods and as previously reported.[9,10] The impact of the cross-linking density on microgel rheological properties was determined with 100% (4-arms), 75% (3-arms), and 50% (2-arms) of the available maleimide groups of 4-arm PEG-Mal cross-linked with SH-PEG-SH (Figure 1A). Microgels formed by this process had similar average diameters determined by optical microscopy, 66 ± 20 μm (4-arms cross-linked), 76 ± 35 μm (3-arms cross-linked), and 72 ± 32 μm (2-arms cross-linked) (Figure 1B,E,G). Frequency and strain sweeps were then performed to determine the linear viscoelastic (LVE) regime of the microgels, and all rheological characterization was conducted after centrifugation of microgels for 5 min at 4000 RCF and removal of the supernatant.[40] Strain and frequency sweeps of all microgel types demonstrated that a frequency of 1 Hz and a strain of 1% were within the LVE regime (Figure 1I,J). With a decrease in the percentage of arms cross-linked to form microgels, a decrease in the average storage modulus was demonstrated from 745 Pa (4-arms cross-linked at 1 Hz and 1% strain) to 449 Pa (3-arms cross-linked at 1 Hz and 1% strain) and 86 Pa (2-arms cross-linked at 1 Hz and 1% strain) (Figure 1I−K). Cyclic strain experiments were then conducted between low (1%, in the LVE regime) and high (500%) strain over 120 and 60 s, respectively, to test the shear thinning and postshear reassembly of the microgels.[10] All of the microgels exhibited a thixotropic behavior, where, following high strains (500%), the microgels are then returned to the starting, higher

https://doi.org/10.1021/acsomega.5c07004
ACS Omega 2026, 11, 746−756

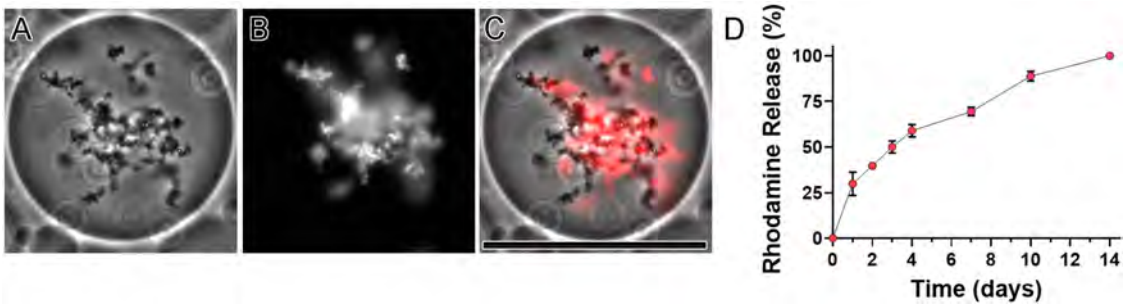

Figure 2. Rhodamine release from microgels. (A) Brightfield image of rhodamine-loaded ssMSNs cross-linked into PEG microgels. (B) Fluorescence of rhodamine loaded in ssMSNs and (C) overlay demonstrating colocalization of rhodamine with ssMSNs (scale = 100 μm). (D) Release of rhodamine from ssMSN microgels. Rhodamine is released over a 2-week timeline from ssMSN-incorporated microgels.

storage modulus upon reapplication of low strain (1%, in the LVE regime; Figure 1K). ssMSN-SH-containing microgels were fabricated similarly to control microgels, except that ssMSN-SH were incorporated with HS-PEG-SH during the fabrication process (Figure 1C). Using the TGA results, ssMSN-SH were added to the HS-PEG-SH solution at a molar ratio that was equal to the amount to cross-link 1-arm of the 4-arm PEG-Mal and HS-PEG-SH used to cross-link either 2 or 3 of the remaining 4-arm PEG-Mal. This resulted in microgels with ssMSN-SH throughout the polymer matrix (Figure 1D,F). The average diameter of the microgels was 60 ± 18 μm for 3-arms cross-linked with HS-PEG-SH and 1-arm with ssMSN-SH and 70 ± 31 μm for 2-arm cross-linked with HS-PEG-SH and 1-arm with ssMSN-SH (Figure 1G). Again, frequency and strain sweeps were then performed to determine the LVE regime of the microgels. Strain and frequency sweeps of all microgel types demonstrated that a frequency of 1 Hz and a strain of 1% was within the LVE regime (Figure 1L,M). With a decrease in the percentage of arms cross-linked to form microgels, a decrease in the storage modulus was demonstrated from 440 Pa (3-arms cross-linked HS-PEG-SH 1-arm ssMSN-SH at 1 Hz and 1% strain) to 83 Pa (2-arms cross-linked HS-PEG-SH 1-arm ssMSN-SH at 1 Hz and 1% strain) (Figure 1L−N). Cyclic strain experiments were then conducted between low (1%, in the LVE regime) and high (500%) strain over 120 and 60 s, respectively, to test the shear thinning and postshear reassembly of the microgels.[10] All of the ssMSN-SH containing microgels exhibited a thixotropic behavior, where, following high strains (500%), the microgels are then returned to the starting, higher storage modulus upon reapplication of low strain (1%, in the LVE regime; Figure 1N). While the chemical cross-linking plays a key role in microgel mechanical properties, the amount of water left between the microgels can also play a role. This is especially true when ssMSN-SH are included, as they will have different affinities for water compared to PEG polymers.

To determine whether the glutathione-degradable nanoparticles could be incorporated into microgels and used to control the release timeline of a drug payload, rhodamine B (rhodB) was used as a model drug. ssMSNs were loaded with rhodB using an evaporation loading technique, followed by conjugation of ssMSN with thiol groups. Rhodamine ssMSN-SH were then incorporated into microgels during fabrication. Overlay images of rhodamine and microgels taken using fluorescence microscopy show that rhodamine remains inside ssMSN-SH after microgel fabrication (Figure 2A−C). When these microgels are incubated in PBS at 37 °C, no release of rhodamine was detected over the two-week observation period. When incubated with glutathione (GSH) at a concentration of 100 mM, ∼25% of rhodamine is released within 1 day, ∼60% within 4 days, and 100% is released by the 14 days time point (Figure 2D). This demonstrates the ability of GSH to degrade the ssMSN-SH incorporated inside the microgels, resulting in rhodamine release that is not observed in PBS.

ssMSN-SH-Cross-Linked MAP Scaffolds. Previous works in MAP scaffolds have reported on polymers to cross-link microgels into MAP scaffolds.[41] Here, MAP scaffolds were fabricated using microgels that have 3-arms of the total 4-arms of PEG-Mal cross-linked (75%), leaving 1-arm of maleimide (25%) available for further cross-linking. 3-arm cross-linked PEG-Mal microgels were centrifuged for 5 min at 4000 RCF to jam them into granular hydrogels. After removal of any supernatant, ssMSN-SH in PBS at a concentration of 2 mg/mL were added to the jammed hydrogels for 15 min to initiate interparticle cross-linking (Figure 3A). This produced MAP scaffolds of microgels cross-linked with ssMSN-SH (Figure 3B−F). Brightfield microscopy images showed ssMSN-SH on the surface of the microgels (Figure 3B), and the cross-linked scaffolds retain their shape (Figure 3C). Scanning electron micrographs show an almost complete coverage of the microgel surfaces with ssMSN-SH (Figure 3D−F). This is in contrast to the micrographs of jammed microgels without MSNs, where there clearly are no MSNs on the surface of the microgels (Figure 1H). SAXS measurements also demonstrate the inclusion of MSNs with microgel structures (Figure S4). Rhodamine-loaded ssMSN-SH were then used to cross-link microgels into MAP scaffolds for fluorescence imaging (Figure 3G). Combining brightfield imaging with fluorescence microscopy demonstrates the extent of ssMSN-SH interparticle cross-linking of microgels (Figure 3H−J). Microgels incorporated with FITC-labeled dextran were cross-linked with rhodamine ssMSN-SH for confocal imaging (Figure 3K). The high-magnification overlay again shows that ssMSN-SH are only on the surface of the microgels and act as interparticle cross-linkers (Figure 3L).

The rheological properties of ssMSN-SH cross-linked MAP scaffolds were determined, and frequency and strain sweeps were performed to determine the LVE. Strain and frequency sweeps demonstrated that a frequency of 1 Hz and a strain of 1% were within the LVE (Figure 3M,N). Interparticle cross-linking of microgels with ssMSN-SH increased the storage modulus from 380 Pa (3-arms cross-linked HS-PEG-SH at 1 Hz and 1% strain) to 1320 Pa (MAP scaffold at 1 Hz and 1% strain) (Figure 3M,N). Cyclic strain experiments were then conducted between low (1%) and high (500%) strain over 120 and 60 s, respectively, to test the shear thinning and postshear

https://doi.org/10.1021/acsomega.5c07004
ACS Omega 2026, 11, 746−756

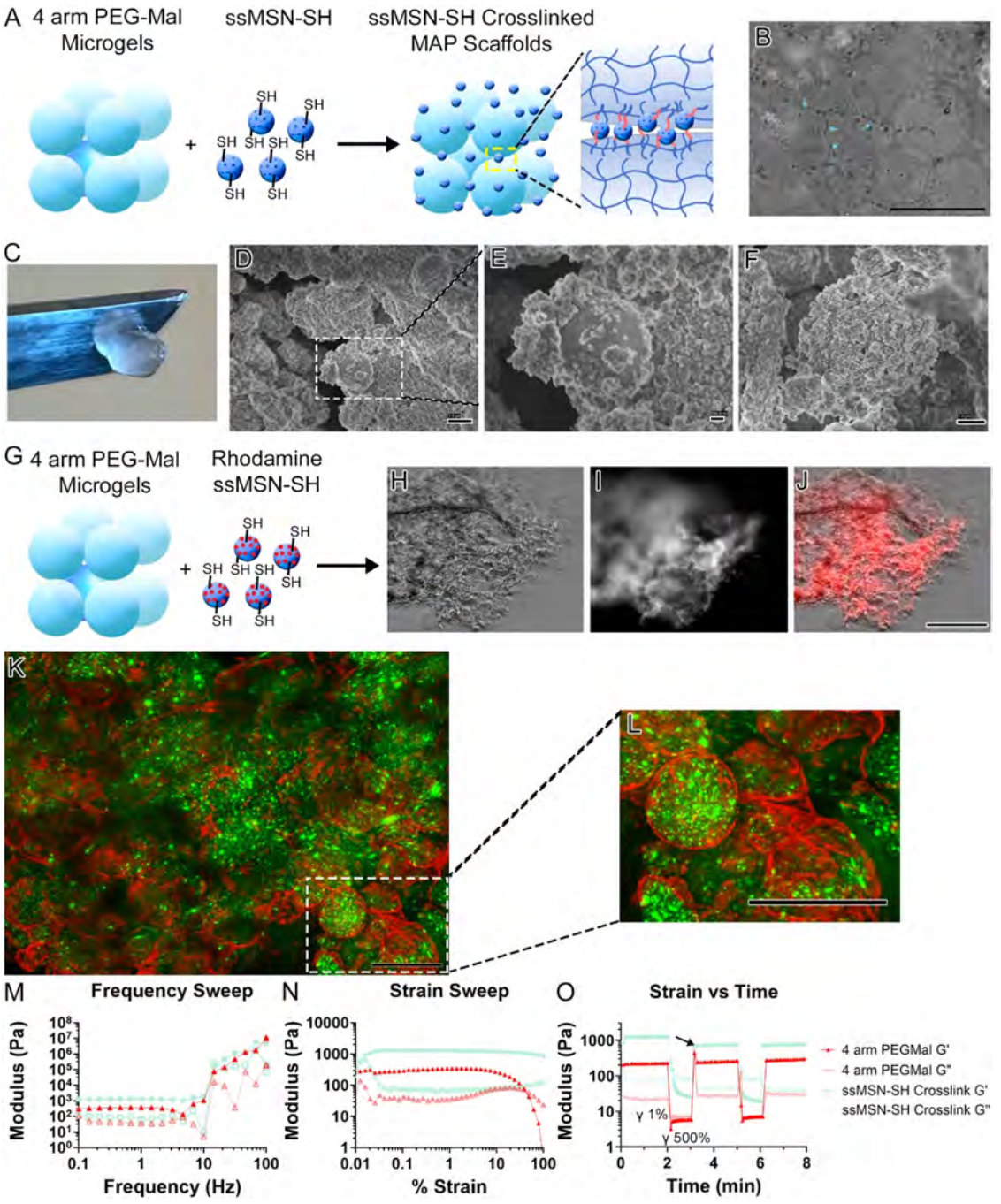

Figure 3. ssMSN-SH-cross-linked MAP scaffolds. (A) Fabrication of ssMSN-cross-linked MAP scaffolds. PEG microgels with uncross-linked maleimide groups are collected via centrifugation, and a solution of thiolated ssMSNs is added to cross-link the microgels into granular hydrogels. (B) Brightfield image depicting cross-linked microgels. Arrows show regions of the granular hydrogels with ssMSNs (scale = 100 μm). (C) ssMSN-cross-linked MAP scaffolds retain their shape after washing and removal from ssMSN solution. (D) Low-magnification (scale = 10 μm) and (E) high-magnification (scale = 200 nm) scanning electron micrographs of ssMSN-cross-linked MAP hydrogel. ssMSNs attach to the surface of the PEG microgels, but are too large to enter the microgel interior. (F) High-magnification image demonstrating a microgel surface completely cross-linked with ssMSNs (scale = 10 μm). (G) Rhodamine-loaded ssMSNs were conjugated with thiol groups and then used to cross-link PEG microgels into MAP scaffolds. (H) Brightfield, (I) rhodamine fluorescence, and (J) overlay showing the structure of a ssMSN-cross-linked MAP scaffold (scale = 200 μm). (K) Confocal fluorescence image of FITC-dextran-incorporated microgels (green) cross-linked into MAP scaffolds with rhodamine-loaded ssMSNs (red). Rhodamine fluorescence is only present on the surface of the microgels, as the ssMSNs do not infiltrate the microgel structure but serve as cross-linkers in the formation of MAP scaffolds (scale = 200 μm). (L) High-magnification image depicting the coverage of microgels with ssMSNs (scale = 200 μm). (M) Frequency and (N) strain sweeps were performed on 3-arm cross-linked microgels and ssMSN-cross-linked MAP hydrogels. Cross-linking microgels into MAP scaffolds increased the storage modulus (G'). (O) Cyclic strain (1% strain at low-strain regions and 500% strain for high-strain regions) demonstrate the thixotropic properties of the 3-arm cross-linked microgels, as they return to their initial storage modulus following increased strain. However, ssMSN-cross-linked MAP hydrogels' storage modulus (G') is decreased following cyclic strain, demonstrating the breakage of the SH-Mal cross-links under high strains.

https://doi.org/10.1021/acsomega.5c07004
ACS Omega 2026, 11, 746−756

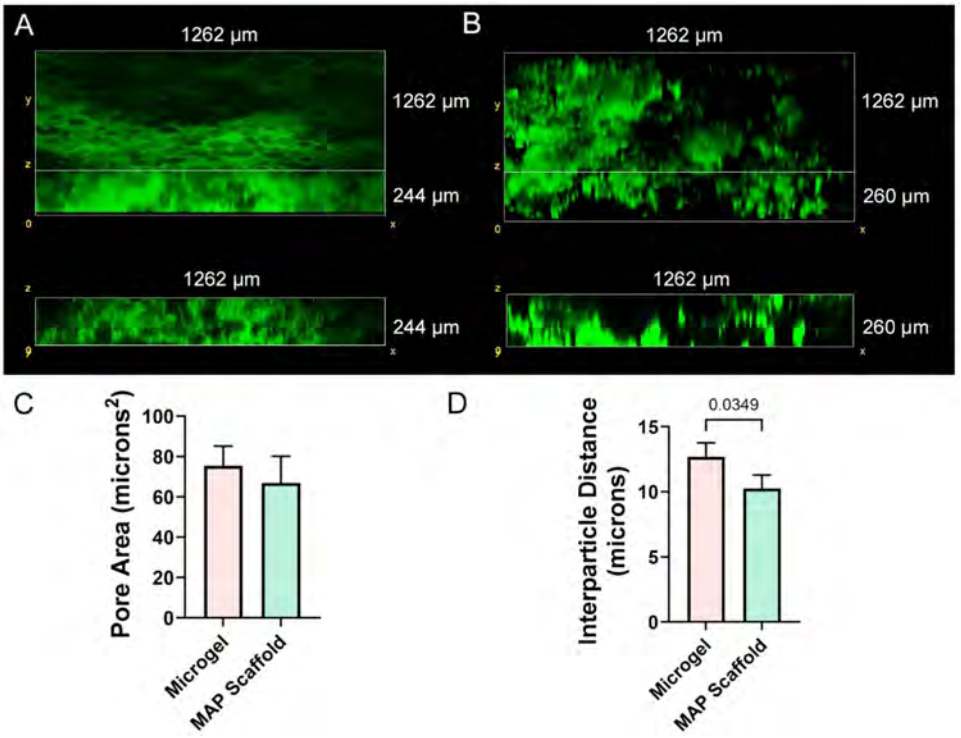

Figure 4. Microgel porosity. (A) Confocal imaging of FITC-labeled dextran throughout centrifuge-packed microgels and (B) ssMSN-cross-linked MAP scaffolds. (C) The pore area is similar following ssMSN cross-linking, but (D) the interparticle distance is significantly reduced following ssMSN cross-linking of microgels.

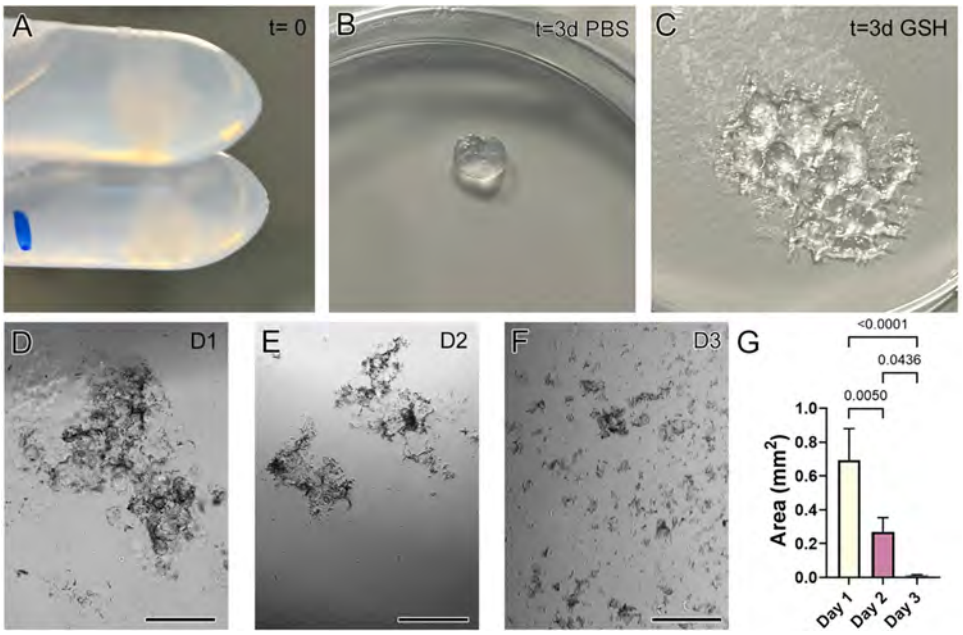

Figure 5. Degradation of ssMSN-SH-cross-linked MAP scaffolds in the presence of glutathione. (A) ssMSN-cross-linked MAP scaffolds were suspended in either (B) control PBS or (C) PBS containing GSH for 3 days. GSH degrades the ssMSNs over time, degrading ssMSN-cross-linked MAP scaffolds and reducing the area of cross-linked microgels from (D) day 1, (E) day 2, and (F) day 3 (scale bars = 500 μm). (G) The area of cross-linked MAP scaffolds is significantly reduced each day.

reassembly of the microgels.[10] The microgels again exhibited a thixotropic behavior, with high strains (500%) reducing the storage modulus of the microgels that is then returned to the starting, higher storage modulus upon reapplication of low strain (1%) (Figure 3O). However, the MAP scaffolds did not return to the same starting storage modulus, and their storage modulus decreased from 1300 to 730 Pa after undergoing 500% strain (Figure 3O). This is due to the irreversible breakage of interparticle cross-links induced by the high strain of the rheometer.

The porosity of jammed microgels and MAP scaffolds was visualized to understand the impact of ssMSN-SH cross-linking

https://doi.org/10.1021/acsomega.5c07004
ACS Omega 2026, 11, 746−756

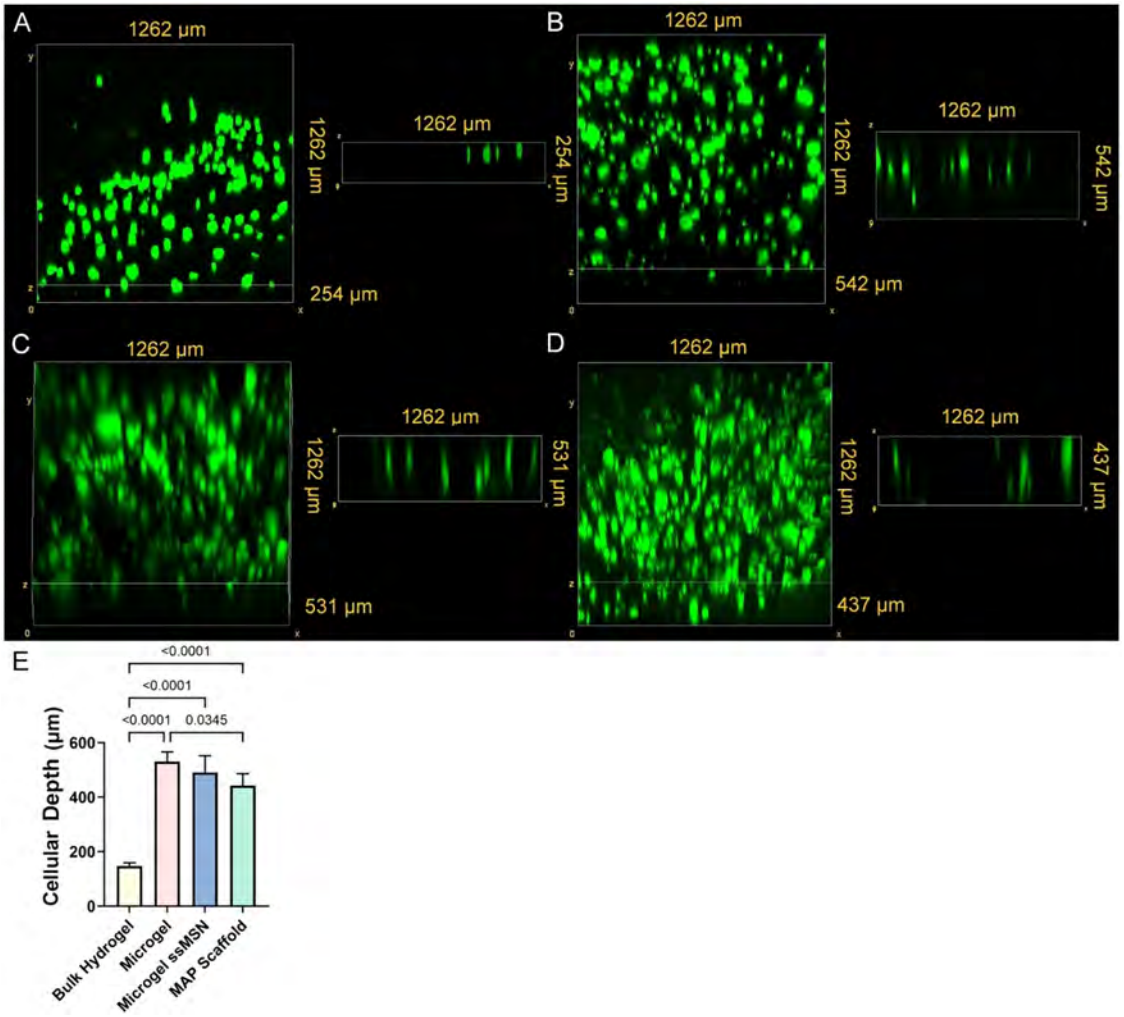

Figure 6. Depth of viable NIH/3T3 fibroblasts into microgels. Confocal micrographs of viable, calcein-labeled NIH3T3 cells were captured on (A) bulk 4-arm PEG hydrogels, (B) centrifuge-packed PEG microgels, (C) centrifuge-packed ssMSN-incorporated PEG microgels, and (D) ssMSN-cross-linked MAP scaffolds. (E) Cells were significantly farther into the packed microgels and ssMSN-cross-linked MAP scaffolds compared with bulk PEG hydrogels.

on porosity. Microgels were jammed via centrifugation for 5 min at 4000 RCF. They were then transferred to a 96-well plate and again centrifuged at 1000 RCF for 5 min to evenly distribute the microgels. ssMSN-SH were added to the wells for 15 min in PBS to allow for the cross-linking reaction to proceed, followed by washing to remove any ssMSN-SH not cross-linked. Fluorescein isothiocyanate-dextran (2000 kDa) was added to the wells to permeate the pores between the microgels as it is too large to permeate into the microgel mesh and remains outside of the microgels. Representative images of microgel controls (Figure 4A) and ssMSN-SH cross-linked MAP scaffolds (Figure 4B) show the permeation of dextran throughout the pores of the scaffolds. There is no significant difference in the pore area between the two groups, with MAP scaffolds having an average pore area of 67.9 ± 13 μm^2 and jammed microgels having an average pore area of 75.5 ± 10 μm^2 (Figure 4C). When the interparticle distance was characterized, it revealed that ssMSN-SH cross-linked MAP scaffolds had a significantly shorter interparticle distance (10.3 ± 1 μm) compared to jammed microgel controls (13 ± 1.1 μm) (Figure 4D). These results show that even though interparticle distances are shorter when microgels are cross-linked into MAP scaffolds, the porosity of the scaffolds remains.

Previously, it has been shown that GSH triggers the degradation of ssMSNs at physiologically relevant concentrations,[18] and this study aimed to capitalize on this property to specifically degrade MAP scaffolds in the presence of GSH. Microgels were cross-linked into MAP scaffolds using ssMSN-SH following centrifuge jamming for 5 min at 4000 RCF, and MAP scaffolds were then suspended in either PBS or PBS with 100 mM GSH (Figure 5A). MAP scaffolds suspended only in PBS at 37 °C retain their structure over the 3 day time period, but when MAP scaffolds are suspended in 100 mM GSH at 37 °C, the ssMSNs degrade, leaving the MAP scaffolds as their component microgels (Figure 5B,C). The area of the ssMSN-SH cross-linked microgels was determined at 1 day, 2 days, and 3 days postincubation in GSH, and significant decreases in area were observed. Following 1 day in GSH, the area of the cross-linked MAP scaffolds was 0.694 ± 0.185 mm^2, which was then reduced to 0.27 ± 0.106 mm^2 after 2 days and to 0.014 ± 0.008 mm^2 after 3 days of degradation in GSH (Figure 5D–G). These experiments demonstrate the engineered degradation of ssMSN-SH MAP scaffolds in the presence of GSH.

https://doi.org/10.1021/acsomega.5c07004
ACS Omega 2026, 11, 746−756

The cellular depth of NIH/3T3 fibroblasts was then analyzed to determine how cells interact with the MAP scaffolds cross-linked with ssMSN-SH. Four different hydrogel scaffolds were tested: (1) bulk 4-arm PEG-Mal hydrogels, (2) centrifuge-packed microgels, (3) centrifuge-packed microgels with incorporated ssMSN-SH (3-arms cross-linked HS-PEG-SH 1-arm ssMSN-SH), and (4) ssMSN-SH cross-linked MAP scaffolds. Confocal microscopy of calcein-labeled NIH/3T3 fibroblasts was used to image live cells over an area of 1262 μm × 1262 μm and depths ranging to 542 μm (Figure 6A−D). Representative images show live, calcein-labeled NIH/3T3 fibroblasts throughout the surface of all of the PEG systems, while images of the x and z axes show the depth of viable cells in the scaffolds. No propidium iodide-labeled (dead) cells were noted, and while high cell viability is expected for microgel biomaterials,[10] the fact that none were visualized is likely due to the washing step prior to imaging. Fibroblasts were visualized at a depth of 147 ± 12 μm after 24 h of culture, which is significantly less than all of the microgel groups (Figure 6E). Viable NIH/3T3 fibroblasts were at similar depths into centrifuge-packed control microgels (530 ± 36 μm) and centrifuge-packed microgels with incorporated ssMSN-SH (490 ± 62 μm). NIH/3T3 fibroblasts were visualized at 442 ± 44 μm into ssMSN-SH-cross-linked MAP scaffolds, which is significantly less than control microgels and significantly more than bulk hydrogels (Figure 6E). The porous space still allows for viable NIH/3T3 fibroblast ssMSN-SH-cross-linked MAP scaffolds to be visualized deeper into the scaffolds compared to bulk hydrogels, where they remain largely on the surface. The presence of ssMSN-SH on the microgel surface and the significantly shorter interparticle distance do have a minor yet statistically significant impact on restricting the depth of visualized viable NIH/3T3 fibroblasts when compared with centrifuge-packed microgels. The incubation of the microgels with DMEM containing 10% FBS, 1% L-glutamine, and 1% penicillin−streptomycin for 1 h prior to seeding likely causes biological factors to interact with the surface of the microgels, but this study does not provide evidence that NIH/3T3 fibroblasts are attaching to the surfaces and actively moving throughout the microgels. However, the microporosity of the ssMSN-SH-cross-linked MAP scaffolds clearly leads to the visualization of viable NIH/3T3 fibroblasts at depths farther from the surface of bulk hydrogels.

CONCLUSIONS

This work provides a solution to the problem of engineering MAP hydrogel properties across length scales by cross-linking PEG-Mal microgels with ssMSN-SH to form MAP scaffolds. We found that ssMSN-SH can be cross-linked inside PEG-Mal microgels, altering microgel mechanical properties and releasing loaded rhodamine when degraded in the presence of GSH. As this work did not address the impact of the SH cross-linking density into the microgels, future studies with different amounts of SH surface groups (including bare ssMSNs) would be important to address how cross-linking densities affect microgel properties. Further, varying GSH concentrations would elucidate the tunability of the payload release from these ssMSN-SH microgels in different environments. Importantly, ssMSN-SH can be used to cross-link PEG-Mal microgels to create MAP scaffolds and increase the storage modulus, maintain microscale porosity, degrade MAP scaffolds into constituent microgels in the presence of GSH, and increase the depth into scaffolds of viable NIH/3T3 fibroblasts. Future studies could look to study the degradation rate by varying GSH concentrations and controlling the amount of ssMSN-SH used to cross-link the scaffolds, imparting even more control on the degradation rate. While others have combined nanoparticles with microgels in various formats,[42−49] this work represents the first example of cross-linking microgels into MAP scaffolds using ssMSN-SH. Here, we demonstrate the ability to use maleimide−thiol cross-linking to readily form these multiscale scaffolds. The modularity of MAP scaffolds has been discussed at length, and here we show that ssMSN-SH can be used to further increase the modularity of MAP scaffolds at the nanoscale. Through cross-linking of MAP scaffolds with ssMSN-SH, the mechanical properties, degradation rate, and interparticle distance can be engineered while maintaining the capability of viable NIH/3T3 fibroblast cells to grow into the MAP scaffolds. Future studies determining cell viability over time with more cell types, especially human-derived cells, and microgels that also present extracellular matrix molecules will further advance the understanding of the utility of these multiscale biomaterials. The ability to engineer different mechanical properties into the MAP scaffolds is important when considering interfacing with different tissues (soft tissue vs bone), while the degradation rate and interparticle distance are important for the timeline of cell growth into MAP scaffolds. Previously, it has been shown that hydrogels cross-linked via maleimide−thiol reactions can degrade over time.[50−52] This added function of ssMSN-SH degradation allows for engineered MAP scaffold degradation, followed by engineering of microgel degradation at a later time. The versatility of the maleimide−thiol cross-linking chemistry will allow most nanoparticle types to act as MAP scaffold cross-linkers if thiol groups can be attached to the nanoparticle surface. Previous research using polymers, specifically linear hyaluronic acid with tetrazine for interparticle cross-linking of hyaluronic acid norbornene microgels, required a similar timeline to cross-link MAP scaffolds (15−30 min) and demonstrated mesenchymal cell viability and growth throughout the MAP scaffolds.[41] The ssMSN-SH-cross-linked MAP scaffolds here increase the functionality, specifically in GSH-triggered MAP scaffold degradation and the ability to load drugs into their mesoporous structure while maintaining scaffold porosity and retaining cellular viability similar to polymer-only systems. However, beyond the scope of this work, we expect that the system can be used to tailor drug release rates by loading therapeutics into either nanoparticles or microgels. Degradation could be engineered by using nanoparticles that demonstrate varying rates of degradation. Cross-linking upon injection can also be envisioned using a dual-chamber syringe with each chamber containing a separate constituent of the hierarchical MAP scaffolds. We envision applications ranging from tissue engineering and regenerative medicine to filtering systems due to the mesopores of MSNs.

ASSOCIATED CONTENT

Supporting Information

The Supporting Information is available free of charge at https://pubs.acs.org/doi/10.1021/acsomega.5c07004.

Nanoparticle characterization (Figure S1); nitrogen adsorption/desorption analysis (Figure S2); thermogra-

https://doi.org/10.1021/acsomega.5c07004
ACS Omega 2026, 11, 746−756

vimetric analysis (Figure S3); and small-angle X-ray scattering microgel analysis (Figure S4) (PDF)

AUTHOR INFORMATION

Corresponding Authors

Jonathan M. Zuidema − *Department of Molecular Biochemistry and Pharmacology, Istituto di Ricerche Farmacologiche Mario Negri "IRCCS", Milan 20156, Italy; Department of Mechanical and Aerospace Engineering, University of Kentucky, Lexington, Kentucky 40506, United States;* orcid.org/0000-0003-2258-0045; Email: jzuidema@uky.edu

Luisa De Cola − *Department of Molecular Biochemistry and Pharmacology, Istituto di Ricerche Farmacologiche Mario Negri "IRCCS", Milan 20156, Italy; Department of Pharmaceutical Sciences, DISFARM, Università degli Studi di Milano, Milan 20133, Italy;* orcid.org/0000-0002-2152-6517; Email: luisa.decola@unimi.it

Authors

Alessandro Ajò − *Department of Molecular Biochemistry and Pharmacology, Istituto di Ricerche Farmacologiche Mario Negri "IRCCS", Milan 20156, Italy; Department of Pharmaceutical Sciences, DISFARM, Università degli Studi di Milano, Milan 20133, Italy;* orcid.org/0000-0003-4049-3818

Marco Carofiglio − *Department of Molecular Biochemistry and Pharmacology, Istituto di Ricerche Farmacologiche Mario Negri "IRCCS", Milan 20156, Italy;* Present Address: Department of Applied Science and Technology, Politecnico di Torino, Turin, Italy

Complete contact information is available at: https://pubs.acs.org/10.1021/acsomega.5c07004

Author Contributions

Research conceptualization and planning and conducting of experiments were performed by J.M.Z. The manuscript was written by J.M.Z. with edits and contributions by all authors. A.A. aided in nanoparticle fabrication and rheological and SAXS characterization. M.C. performed cell culture experiments and contributed to confocal imaging. All authors have given approval to the final version of the manuscript.

Funding

This project received funding through the European Union's Horizon 2021 research and innovation program under the Marie Skłodowska-Curie Grant Agreement No. 101067770 ("PACMAN"). J.M.Z. undertook this work as a Marie Skłodowska-Curie fellow. J.M.Z. is a Lighthouse Beacon Foundation Scholar. L.D.C. thanks Next Gen EU and MUR, Project PNRR M4C2, "Mano-HCC", PE_00000019, HEAL ITALIA, CUP E93C22001860006 for support.

Notes

The authors declare no competing financial interest.

ACKNOWLEDGMENTS

The authors would like to thank Nadia Santo from the NOLIMITS platform of microscopy, at the University of Milan, for her expert assistance in acquiring the scanning electron microscopy (SEM) images.

REFERENCES

(1) Daly, A. C.; Riley, L.; Segura, T.; Burdick, J. A. Hydrogel microparticles for biomedical applications. *Nat. Rev. Mater.* **2020**, *5* (1), 20−43.

(2) Daly, A. C. Granular Hydrogels in Biofabrication: Recent Advances and Future Perspectives. *Adv. Healthcare Mater.* **2024**, *13* (25), No. 2301388.

(3) Jaberi, A.; Kedzierski, A.; Kheirabadi, S.; Tagay, Y.; Ataie, Z.; Zavari, S.; Naghashnejad, M.; Waldron, O.; Adhikari, D.; Lester, G.; et al. Engineering Microgel Packing to Tailor the Physical and Biological Properties of Gelatin Methacryloyl Granular Hydrogel Scaffolds. *Adv. Healthcare Mater.* **2024**, *13* (25), No. 2402489.

(4) Charlet, A.; Bono, F.; Amstad, E. Mechanical reinforcement of granular hydrogels. *Chem. Sci.* **2022**, *13* (11), 3082−3093.

(5) Riley, L.; Schirmer, L.; Segura, T. Granular hydrogels: emergent properties of jammed hydrogel microparticles and their applications in tissue repair and regeneration. *Curr. Opin. Biotechnol.* **2019**, *60*, 1−8.

(6) Qazi, T. H.; Muir, V. G.; Burdick, J. A. Methods to Characterize Granular Hydrogel Rheological Properties, Porosity, and Cell Invasion. *ACS Biomater. Sci. Eng.* **2022**, *8* (4), 1427−1442.

(7) Darling, N. J.; Xi, W. X.; Sideris, E.; Anderson, A. R.; Pong, C.; Carmichael, S. T.; Segura, T. Click by Click Microporous Annealed Particle (MAP) Scaffolds. *Adv. Healthcare Mater.* **2020**, *9* (10), No. 201901391, DOI: 10.1002/adhm.201901391.

(8) Widener, A. E.; Roberts, A.; Phelps, E. A. Single versus dual microgel species for forming guest-host microporous annealed particle PEG-MAL hydrogel. *J. Biomed. Mater. Res. A* **2023**, *111* (9), 1379−1389.

(9) Widener, A. E.; Duraivel, S.; Angelini, T. E.; Phelps, E. A. Injectable Microporous Annealed Particle Hydrogel Based on Guest-Host-Interlinked Polyethylene Glycol Maleimide Microgels. *Adv. Nanobiomed. Res.* **2022**, *2* (10), No. 2200030, DOI: 10.1002/anbr.202200030.

(10) Widener, A. E.; Bhatta, M.; Angelini, T. E.; Phelps, E. A. Guest-host interlinked PEG-MAL granular hydrogels as an engineered cellular microenvironment. *Biomater. Sci.* **2021**, *9* (7), 2480−2493.

(11) Caldwell, A. S.; Campbell, G. T.; Shekiro, K. M. T.; Anseth, K. S. Clickable Microgel Scaffolds as Platforms for 3D Cell Encapsulation. *Adv. Healthcare Mater.* **2017**, *6* (15), No. 1700254, DOI: 10.1002/adhm.201700254.

(12) Morillas-Becerill, L.; De Cola, L.; Zuidema, J. M. Inorganic Nanoparticle Empowered Biomaterial Hybrids: Engineered Payload Release. *Front. Nanotechnol.* **2022**, *4*, No. 999923.

(13) Arif, M. Noble metal nanoparticles encapsulated smart microgels: A critical review. *J. Mol. Liq.* **2024**, *403*, No. 124869.

(14) Oberdisse, J.; Hellweg, T. Recent advances in stimuli-responsive core-shell microgel particles: synthesis, characterisation, and applications. *Colloid Polym. Sci.* **2020**, *298* (7), 921−935.

(15) Kankala, R. K.; Han, Y. H.; Na, J.; Lee, C. H.; Sun, Z. Q.; Wang, S. B.; Kimura, T.; Ok, Y. S.; Yamauchi, Y.; Chen, A. Z.; Wu, K. C. Nanoarchitectured Structure and Surface Biofunctionality of Mesoporous Silica Nanoparticles. *Adv. Mater.* **2020**, *32* (23), No. 1907035.

(16) Wu, S. H.; Mou, C. Y.; Lin, H. P. Synthesis of mesoporous silica nanoparticles. *Chem. Soc. Rev.* **2013**, *42* (9), 3862−3875.

(17) Wen, J.; Yang, K.; Liu, F. Y.; Li, H. J.; Xu, Y. Q.; Sun, S. G. Diverse gatekeepers for mesoporous silica nanoparticle based drug delivery systems. *Chem. Soc. Rev.* **2017**, *46* (19), 6024−6045.

(18) Prasetyanto, E. A.; Bertucci, A.; Septiadi, D.; Corradini, R.; Castro-Hartmann, P.; De Cola, L. Breakable Hybrid Organosilica Nanocapsules for Protein Delivery. *Angew. Chem., Int. Ed.* **2016**, *55* (10), 3323−3327.

(19) Croissant, J.; Cattoën, X.; Man, M. W. C.; Gallud, A.; Raehm, L.; Trens, P.; Maynadier, M.; Durand, J. O. Biodegradable Ethylene-Bis(Propyl)Disulfide-Based Periodic Mesoporous Organosilica Nanorods and Nanospheres for Efficient In-Vitro Drug Delivery. *Adv. Mater.* **2014**, *26* (35), 6174.

(20) Picchetti, P.; DiMarco, B. N.; Travaglini, L.; Zhang, Y.; Ortega-Liebana, M. C.; De Cola, L. Breaking with Light: Stimuli-Responsive

Mesoporous Organosilica Particles. *Chem. Mater.* **2020**, *32* (1), 392−399.
(21) Picchetti, P.; Volpi, S.; Rossetti, M.; Dore, M. D.; Trinh, T.; Biedermann, F.; Neri, M.; Bertucci, A.; Porchetta, A.; Corradini, R.; et al. Responsive Nucleic Acid-Based Organosilica Nanoparticles. *J. Am. Chem. Soc.* **2023**, *145* (42), 22896−22902.
(22) Wu, L. T.; Pan, H.; Huang, W. L.; Wang, M. J.; Hu, Z. X.; Zhang, F. Self-assembled degradable iron-doped mesoporous silica nanoparticles for the smart delivery of prochloraz to improve plant protection and reduce environmental impact. *Environ. Technol. Innovations* **2022**, *28*, No. 102890.
(23) Hurley, M. T.; Wang, Z. F.; Mahle, A.; Rabin, D.; Liu, Q.; English, D. S.; Zachariah, M. R.; Stein, D.; DeShong, P. Synthesis, Characterization, and Application of Antibody Functionalized Fluorescent Silica Nanoparticles. *Adv. Funct. Mater.* **2013**, *23* (26), 3335−3343.
(24) Hu, Z. X.; Tan, J. T.; Lai, Z. Q.; Zheng, R.; Zhong, J. H.; Wang, Y. W.; Li, X. X.; Yang, N.; Li, J. P.; Yang, W.; et al. Aptamer Combined with Fluorescent Silica Nanoparticles for Detection of Hepatoma Cells. *Nanoscale Res. Lett.* **2017**, *12*, 96.
(25) Pan, L. M.; He, Q. J.; Liu, J. N.; Chen, Y.; Ma, M.; Zhang, L. L.; Shi, J. L. Nuclear-Targeted Drug Delivery of TAT Peptide-Conjugated Monodisperse Mesoporous Silica Nanoparticles. *J. Am. Chem. Soc.* **2012**, *134* (13), 5722−5725.
(26) Choi, W.; Kohane, D. S. Hybrid Nanoparticle-Hydrogel Systems for Drug Delivery Depots and Other Biomedical Applications. *ACS Nano* **2024**, *18* (34), 22780−22792.
(27) Piantanida, E.; Alonci, G.; Bertucci, A.; De Cola, L. Design of Nanocomposite Injectable Hydrogels for Minimally Invasive Surgery. *Acc. Chem. Res.* **2019**, *52* (8), 2101−2112.
(28) Alonci, G.; Fiorini, F.; Riva, P.; Monroy, F.; Lopez-Montero, I.; Perretta, S.; De Cola, L. Injectable Hybrid Hydrogels, with Cell-Responsive Degradation, for Tumor Resection. *ACS Appl. Bio Mater.* **2018**, *1* (5), 1301−1310.
(29) Li, Y.; Chen, X.; Jin, R. H.; Chen, L.; Dang, M.; Cao, H.; Dong, Y.; Cai, B. L.; Bai, G.; Gooding, J. J.; et al. Injectable hydrogel with MSNs/microRNA-21−5p delivery enables both immunomodification and enhanced angiogenesis for myocardial infarction therapy in pigs. *Sci. Adv.* **2021**, *7* (9), No. eabd6740.
(30) Hu, Y.; Dong, X. Y.; Ke, L.; Zhang, S. W.; Zhao, D.; Chen, H.; Xiao, X. C. Polysaccharides/mesoporous silica nanoparticles hybrid composite hydrogel beads for sustained drug delivery. *J. Mater. Sci.* **2017**, *52* (6), 3095−3109.
(31) Zengin, A.; Castro, J. P. O.; Habibovic, P.; van Rijt, S. H. Injectable, self-healing mesoporous silica nanocomposite hydrogels with improved mechanical properties. *Nanoscale* **2021**, *13* (2), 1144−1154.
(32) Piantanida, E.; Boskoski, I.; Quero, G.; Gallo, C.; Zhang, Y.; Fiorillo, C.; Arena, V.; Costamagna, G.; Perretta, S.; De Cola, L. Nanocomposite hyaluronic acid-based hydrogel for the treatment of esophageal fistulas. *Mater. Today Bio* **2021**, *10*, No. 100109.
(33) Zengin, A.; Hafeez, S.; Habibovic, P.; Baker, M.; van Rijt, S. Extracellular matrix mimetic supramolecular hydrogels reinforced with covalent crosslinked mesoporous silica nanoparticles. *J. Mater. Chem. B* **2024**, *12*, 12577.
(34) Bakaic, E.; Smeets, N. M. B.; Hoare, T. Injectable hydrogels based on poly(ethylene glycol) and derivatives as functional biomaterials. *RSC Adv.* **2015**, *5* (45), 35469−35486.
(35) Shi, J. Y.; Yu, L.; Ding, J. D. PEG-based thermosensitive and biodegradable hydrogels. *Acta Biomater.* **2021**, *128*, 42−59.
(36) Darling, N. J.; Hung, Y. S.; Sharma, S.; Segura, T. Controlling the kinetics of thiol-maleimide Michael-type addition gelation kinetics for the generation of homogenous poly(ethylene glycol) hydrogels. *Biomaterials* **2016**, *101*, 199−206.
(37) Jansen, L. E.; Negrón-Piñeiro, L. J.; Galarza, S.; Peyton, S. R. Control of thiol-maleimide reaction kinetics in PEG hydrogel networks. *Acta Biomater.* **2018**, *70*, 120−128.
(38) Headen, D. M.; Aubry, G.; Lu, H.; García, A. J. Microfluidic-Based Generation of Size-Controlled, Biofunctionalized Synthetic Polymer Microgels for Cell Encapsulation. *Adv. Mater.* **2014**, *26* (19), 3003−3008.
(39) Maggini, L.; Travaglini, L.; Cabrera, I.; Castro-Hartmann, P.; De Cola, L. Biodegradable Peptide-Silica Nanodonuts. *Chem. − Eur. J.* **2016**, *22* (11), 3697−3703.
(40) Zuidema, J. M.; Rivet, C. J.; Gilbert, R. J.; Morrison, F. A. A protocol for rheological characterization of hydrogels for tissue engineering strategies. *J. Biomed. Mater. Res. B* **2014**, *102* (5), 1063−1073.
(41) Anderson, A. R.; Nicklow, E.; Segura, T. Particle fraction is a bioactive cue in granular scaffolds. *Acta Biomater.* **2022**, *150*, 111−127.
(42) Vialetto, J.; Ramakrishna, S. N.; Stock, S.; von Klitzing, R.; Isa, L. Modulating the conformation of microgels by complexation with inorganic nanoparticles. *J. Colloid Interface Sci.* **2024**, *672*, 797−804.
(43) Liu, Y. S.; Yao, J.; Deng, G. T.; Zhong, G.; Zhao, J. P.; Lan, Q. M.; Meng, J. Z.; Yu, Y.; Chen, F. Microgel Encapsulated Nanoparticles for Intra-articular Disulfiram Delivery to Treat Osteoarthritis. *Mol. Pharmaceutics* **2024**, *21* (1), 87−101.
(44) Song, X. Y.; Zhou, J. Z.; Qiao, C. Z.; Xu, X. F.; Zhao, S. L.; Liu, H. L. Engulfing Behavior of Nanoparticles into Thermoresponsive Microgels: A Mesoscopic Simulation Study. *J. Phys. Chem. B* **2021**, *125* (11), 2994−3004.
(45) Dagdelen, S.; Mackiewicz, M.; Osial, M.; Waleka-Bargiel, E.; Romanski, J.; Krysinski, P.; Karbarz, M. Redox-responsive degradable microgel modified with superparamagnetic nanoparticles exhibiting controlled, hyperthermia-enhanced drug release. *J. Mater. Sci.* **2023**, *58* (9), 4094−4114.
(46) Rahman, S.; Al-Harbi, F. F.; Ajmal, M.; Naseem, A.; Farooqi, Z. H.; Siddiq, M. Engineering of micron-sized spherical anionic microgel fabricated with silver nanoparticles with antimicrobial and catalytic potential. *J. Mater. Sci.* **2022**, *57* (12), 6763−6779.
(47) Sabadasch, V.; Dirksen, M.; Fandrich, P.; Cremer, J.; Biere, N.; Anselmetti, D.; Hellweg, T. Pd Nanoparticle-Loaded Smart Microgel-Based Membranes as Reusable Catalysts. *ACS Appl. Mater. Interfaces* **2022**, *14*, 49181.
(48) Kakar, M. U.; Khan, K.; Akram, M.; Sami, R.; Khojah, E.; Iqbal, I.; Helal, M.; Hakeem, A.; Deng, Y. L.; Dai, R. J. Synthesis of bimetallic nanoparticles loaded on to PNIPAM hybrid microgel and their catalytic activity. *Sci. Rep.* **2021**, *11* (1), No. 14759.
(49) Erning, K.; Wilson, K. L.; Smith, C. S.; Nguyen, L.; Joseph, N. I.; Irengo, R.; Cao, L. Y.; Cumaran, M.; Shi, Y.; Lyu, S.; et al. Delivery of Angiogenic Therapy from Flowable Hyaluronic Acid Porous Scaffolds Results in Functional Improvement without Anti-Inflammatory Agents. *Adv. Funct. Mater.* **2025**, *35*, No. 2500696, DOI: 10.1002/adfm.202500696.
(50) Hebner, T. S.; Kirkpatrick, B. E.; Fairbanks, B. D.; Bowman, C. N.; Anseth, K. S.; Benoit, D. S. W. Radical-Mediated Degradation of Thiol-Maleimide Hydrogels. *Adv. Sci.* **2024**, *11* (25), No. 2402191.
(51) Wu, H.; LeValley, P. J.; Luo, T.; Kloxin, A. M.; Kiick, K. L. Manipulation of Glutathione-Mediated Degradation of Thiol-Maleimide Conjugates. *Bioconjugate Chem.* **2018**, *29* (11), 3595−3605.
(52) Baldwin, A. D.; Kiick, K. L. Tunable degradation of maleimide-thiol adducts in reducing environments. *Bioconjugate Chem.* **2011**, *22* (10), 1946−1953.

https://doi.org/10.1021/acsomega.5c07004
ACS Omega 2026, 11, 746−756